

On the structure of high-pressure supercooled and glassy water

Riccardo Foffi and Francesco Sciortino

Department of Physics, Sapienza Università di Roma, Piazzale Aldo Moro, 2, 00185 Rome, Italy

(Dated: September 21, 2021)

We numerically investigate the metastable equilibrium structure of deep supercooled and glassy water under pressure, covering the range of densities corresponding to the experimentally produced high-density and very-high-density amorphous phases. At $T = 188$ K, a continuous increase in density is observed on varying pressure from 2.5 to 13 kbar, with no signs of first-order transitions. Exploiting a recently proposed approach to the analysis of the radial distribution function — based on topological properties of the hydrogen-bond network — we are able to identify well-defined local geometries that involve pair of molecules separated by multiple hydrogen bonds, specific of the high and very high density structures.

The structure of the different amorphous forms of water, their interconversions and their connection to the liquid state are fascinating topics, which keep capturing the attention of the scientific community [1–5]. One of these amorphous states, the low-density amorphous ice (LDA), can be generated via a multiplicity of processes (vapour deposition [6], hyper-quenching [7], heating/decompression of other disordered forms of ice [8]) and it is now well characterised [2, 9, 10]. LDA has a density $\rho = 0.94 \text{ g cm}^{-3}$ at ambient pressure (P) and temperature $T = 80$ K, and it is characterised by locally tetrahedral structures in which each molecule accepts and donates two hydrogen bonds (HBs), the disordered equivalent of ice I [3]. The results on the high-density forms of amorphous water, for which density and structure seem to be somehow dependent on production process and annealing protocols, are much more controversial. The most recent picture describes two variants of high-density amorphous ice (HDA), called un-annealed HDA (uHDA) and expanded HDA (eHDA), characterised by similar densities ρ_{HDA} , 1.15 and 1.13 g cm^{-3} respectively, along with a third form, the very-high-density amorphous ice (VHDA) with $\rho_{\text{VHDA}} = 1.26 \text{ g cm}^{-3}$. uHDA is the material resulting from compression of ice I_h at 77 K to above GPa pressures [11], while eHDA can be obtained, among other methods, from the decompression of VHDA at 140 K to pressures lower than ≈ 0.1 GPa [8]. Despite their structural similarities, eHDA appears to have a significantly enhanced thermal stability with respect to uHDA [12, 13]. VHDA can be prepared either from ice I_h by pressure-induced amorphization above 1.2 GPa at temperatures $130 < T < 150$ K [14] or by annealing uHDA to $T > 160$ K at GPa pressures [15]. More details on the preparation routes of amorphous states can be found in recent reviews [4, 16, 17].

Recent experimental results show that eHDA can be reversibly transformed into VHDA, suggesting that despite significant structural differences eHDA and VHDA might be linked to one another via a continuous thermodynamic path [18]. In other experiments a seemingly jump-like transition between HDA and VHDA was instead identified [19–21].

Experimental and numerical investigations have established that the most prominent structural difference between the low- and high-density forms of amorphous water is an inward collapse of the second hydration shell, a transformation that mimics the structural changes observed upon compression in the liquid state [22–25]. Less understood are the differences between HDA and VHDA; a further collapse of the second shell has been clearly observed experimentally [23, 26, 27], but it is not clear if additional novel structural features exist that distinguish VHDA from HDA. Also, a more general question concerns whether, and to what extent, VHDA and HDA actually behave as distinct materials. This Letter focuses exactly on these two points: (a) how can we interpret the structural changes and (b) are eHDA and VHDA separated by a first order transition? We find that the simulated liquid explores configurations that accurately mimic the structural changes observed experimentally between HDA and VHDA, implying a deep connection between pressure-prepared amorphous ice and deeply supercooled water [25], oppositely to conclusions reported in other studies [28, 29]. We also find that at such low T the equation of state does not show any unstable region in this density range, consistent with the hypothesis of a continuity of states between eHDA and VHDA. Finally, we characterise the structural crossover from HDA to VHDA by identifying a connection between specific local geometries and topological properties of the HB network, providing a quantitative characterization of what is generically (and possibly improperly) referred to as the collapse of the second neighbour shell.

A typical experimental procedure to generate HDA and VHDA requires the compression of ice I_h at low T , which transforms, via a mechanical instability [30], into a disordered material that is later recovered at ambient P . Repeating this process on the computer, while often numerically implemented [25, 31–35] requires pressure rates significantly faster than the experimental counterpart, allowing for the possibility that the resulting configurations heavily depend on the protocol. Our numerical approach to generate glass samples exploits the picture of the glass as a quenched liquid. We investigate high-density liq-

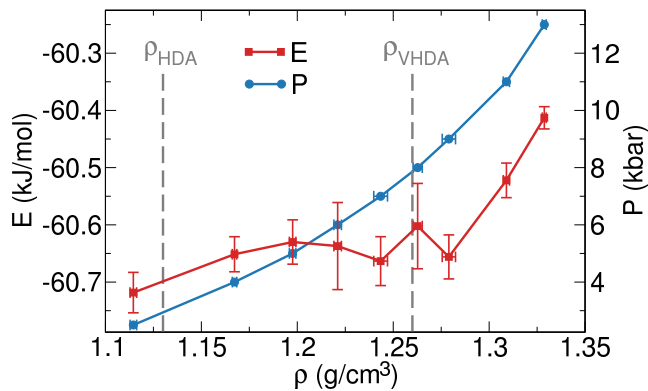


FIG. 1. Thermodynamics of TIP4P/Ice water from MD simulations along the 188 K isotherm. Equation of state (right y -axis) and potential energy (per molecule, left y -axis) as a function of density. Grey dashed lines show the eHDA and VHDA experimental ρ at 80 K and 1 bar for reference. Error bars are estimated as the variance of the averages over 10 distinct time intervals in the production run.

uid configurations of TIP4P/Ice water [36] along a cold ($T = 188$ K) isotherm, right below the model liquid-liquid critical temperature $T_c = 188.6$ K [37], from 2.5 to 13 kbar, corresponding to a density range from 1.1 to 1.3 g cm^{-3} . The results for 2.5 and 4 kbar are reproduced from Ref. [38]. Performing novel numerical simulations longer than 10–25 μs , it is still possible to reach (metastable) equilibrium at this T , eliminating any concern of history dependence and out-of-equilibrium effects. The associated glass structures are provided by the inherent structures (IS), the local energy minima reached via a constant-volume steepest descent procedure which removes vibrational distortions [39]. All the numerical procedures are discussed in detail in the S.M. (which includes Refs. [40–47]).

Figure 1 shows the potential energy (per molecule) E as a function of density (ρ) and the equation of state P vs. ρ at $T = 188$ K. In the explored range, $P(\rho)$ has positive concavity and no discontinuities, establishing the absence of any thermodynamic transition between two distinct dense liquid forms along this isotherm. Quite interesting, however, is the density dependence of the potential energy E , which shows a region between 1.12 and 1.25 g cm^{-3} (the typical density values of eHDA and VHDA) in which E weakly depends on ρ , suggesting that the structural changes taking place on increasing pressure have a small energetic cost. Only beyond ρ_{VHDA} , E grows significantly with ρ .

Fig. 2 shows the continuous smooth evolution of the calculated oxygen-oxygen radial distribution function $g(r)$. On increasing P , the concentration of interstitial molecules ($r \approx 3.2 - 3.5 \text{ \AA}$) increases significantly, while the tetrahedral peak ($r \approx 4.4 \text{ \AA}$) is suppressed. Two additional features characterise the evolution: the devel-

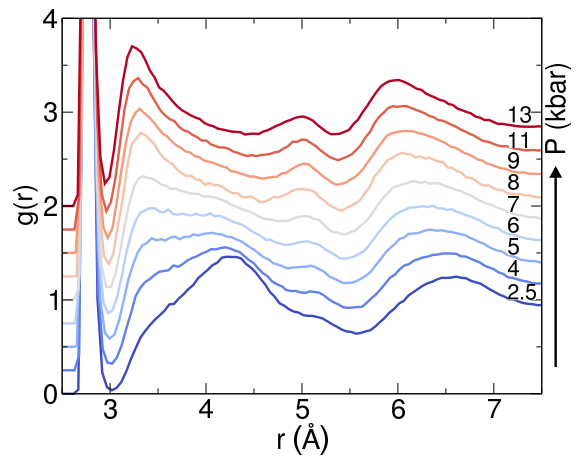


FIG. 2. Oxygen-oxygen radial distribution function evaluated in the IS along the 188 K isotherm from 2.5 to 13 kbar. The evaluation of the spatial correlations in the IS highlights the evolution of the structural features. Successive $g(r)$ curves are shifted by 0.25 on the vertical axis

opment of a novel peak at $r \approx 5 \text{ \AA}$ and the intensity crossover from $r \approx 6.7 \text{ \AA}$ to $\approx 6 \text{ \AA}$. The corresponding evolution of the structure factor [48] is reported in the S.M.

Before interpreting the structural features, we validate the numerical results comparing the structure of the glasses generated by quenching equilibrium liquid configurations with available experimental data of eHDA and VHDA structures from Mariedahl *et al.* [23] and Bowron *et al.* [9]. To do so, we quench configurations equilibrated at $T = 188$ K and different P to $T = 80$ K and ambient pressure — the same T and P in Refs [9, 23]. Following a short MD simulation, the density and the vibrational and rotational degrees of freedom adjust to $T = 188$ K and $P = 1$ bar. More details can be found in the S.M. Since classical calculations neglect the quantum delocalization of the atoms [49, 50], the height of the first peak of $g(r)$ is usually overestimated. To include in an effective way the quantum broadening of O–O distances (as well as any possible broadening due to the experimental procedures) we have convoluted the numerical $g(r)$ with a gaussian of variance $\sigma_B^2 = 7.1 \times 10^{-3} \text{ \AA}^2$, a value obtained by matching the heights of the first peak in the numerical $g(r)$ to the experimental values. This value is consistent with the broadening observed between path-integral and classical simulations of the same model [50]. Note that the implemented broadening becomes irrelevant when $r \gg \sigma_B$ (Fig. S8 reports the comparison without the correction). We compare the experimental data (which display some differences, possibly due to different preparation histories) to numerical $g(r)$ s with ρ s comparable to experimental values typical of HDA and VHDA. Fig. 3 shows that both eHDA and VHDA radial features are rather faithfully reproduced by TIP4P/Ice. The quality of the com-

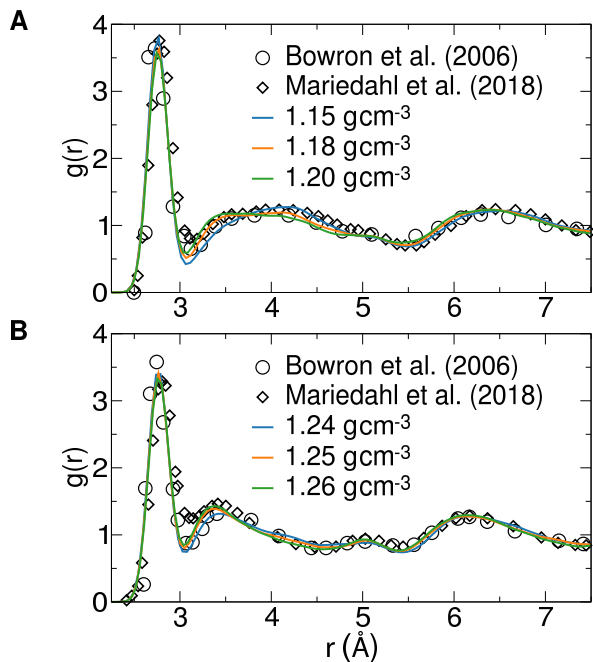


FIG. 3. Comparison between experimental (symbols) and numerical (lines) $g(r)$ in (a) eHDA and (b) VHDA at $T = 80$ K and $P = 1$ bar. The densities indicated in the label refer to the values at ambient pressure.

parison enforces our confidence in the TIP4P/Ice model to properly describe the local geometries responsible for the structural signatures observed experimentally, as detailed in the following analysis.

To gain a better insight in the structural changes on going from eHDA to VHDA we adopt a methodology recently proposed to investigate the liquid-liquid phase transition [38]. We separate the contributions to the $g(r)$ originating from pairs of molecules with “chemical distance” D , where D is defined as the minimum number of HBs connecting the two molecules along the HB network. An analysis based on the HB network topology depends crucially on the ability to properly identify HBs. In TIP4P/Ice, HBs can be accurately identified at all pressures (Figs. S9–S11) adopting the Luzar-Chandler definition [51]. Furthermore, at all explored densities, more than 99.5% of the H atoms are involved in HBs, indicating that practically all molecules donate two hydrogens for bonding (Fig. S12).

We connect structure and network topology by writing

$$g(r) = \sum_D g_D(r) \quad (1)$$

where $g_D(r)$ is the radial distribution function evaluated among only pairs of molecules at chemical distance D . The effects of this decomposition are shown for the lowest and highest studied P (2.5 and 13 kbar) in Fig. 4. The partitioning reveals precise relationships between spatial

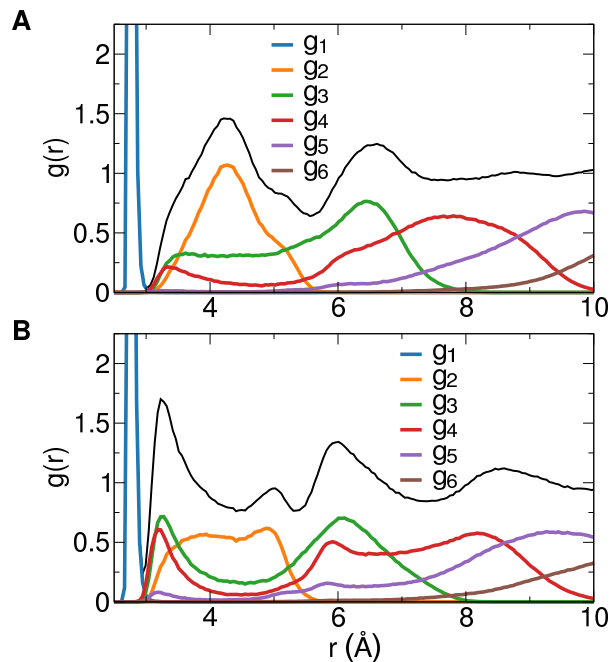


FIG. 4. Radial distribution function of water (evaluated in the IS) at 188 K and P (a) 2.5 kbar and (b) 13 kbar separated in their g_D contributions ($1 \leq D \leq 6$) from pairs of molecules at chemical distance D . The black line is the sum over all $g_D(r)$, equal to the total $g(r)$ (Eq. 1).

and topological features, providing insight into the structural evolution that occurs upon compression and thus facilitating a classification of molecule pairs into distinct groups. First, we observe well defined peaks at $r \leq 3.5$ Å for $D = 3, 4$ and 5 , clarifying that interstitial molecules, despite their close real-space distance, reaching down to $r \approx 3$ Å, are separated by three or more HBs. The growth in the number of interstitial molecules, (a phenomenon which characterizes the transition from the low to the high density liquid [38]) is significantly enhanced on going from HDA-like to VHDA-like densities. Figure 4 also shows that the peak at $r \approx 5$ Å can be associated to molecules separated only by two HBs ($D = 2$) and that the peak at $r \approx 6$ Å originates from pairs with chemical distance $D = 4$. Indeed, while $D = 3$ provides a major contribution to $g(r \approx 6$ Å), only in $D = 4$ a new peak arises, continuously growing upon compression from high to very-high densities.

Finally, $g_2(r)$ shows a complete disappearance of the tetrahedral peak at 4.4 Å — the landmark of the LDL phase, still quite intense in the HDL at coexistence [38] — which progressively transforms into a broad featureless distribution, indicating a significant broadening of the $\text{O}\ddot{\text{O}}\text{O}$ angle of H-bonded triplets of molecules.

To pin down the local geometries responsible for the peaks, $g_D(r)$ can be further decomposed into contributions from “rings” of different length [38]. To each pair of molecules contributing to $g(r)$ we now associate, in ad-

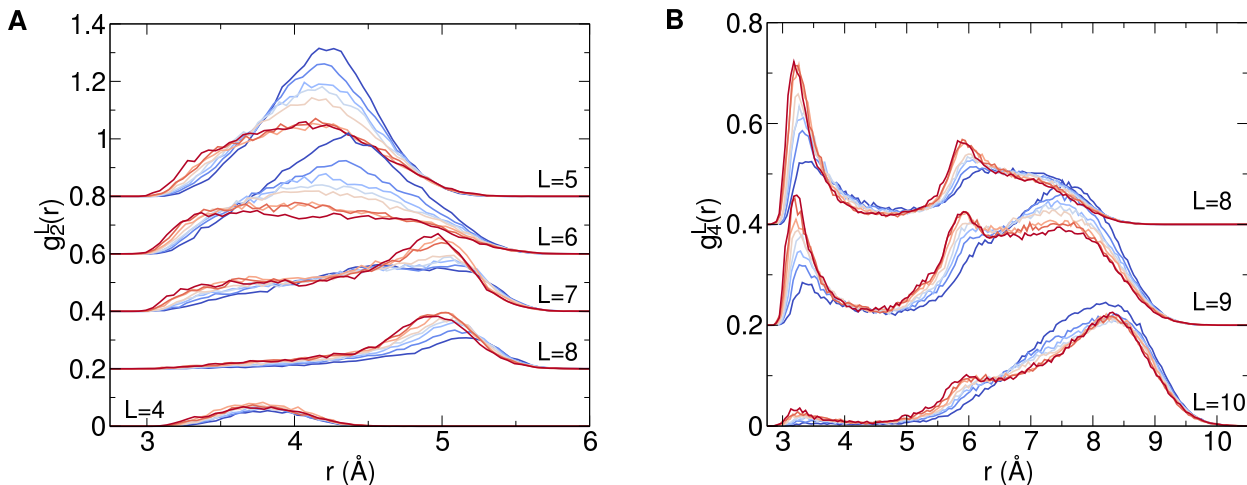


FIG. 5. Contribution to the radial distribution function from pairs of molecules at (a) $D=2$ and (b) $D=4$, separated according to the ring length L , along the $T = 188$ K isotherm. Colours from red to blue indicate increasing pressure from 2.5 to 13 kbar. Note that for $D = 2$ and $L = 7$ and 8 , a clear peak progressively grows at $r \approx 5$ Å. Also note that for $D = 4$, beside the growth at the interstitial distance $r \approx 3.2$ Å a further peak appears at $r \approx 6$ Å, most clearly for $L = 8$ and $L = 9$.

dition to the spatial distance r and chemical distance D , also a ring length L . The ring is selected by joining the two shortest non-intersecting HB-paths connecting the selected pair (see also Fig. S15 for an example). Then each g_D can be written as

$$g_D(r) = \sum_L g_D^L(r) \quad (2)$$

where g_D^L indicates the contribution to $g(r)$ from all pairs of molecules with chemical distance D and ring length L .

This analysis applied to $g_2(r)$, detailed in Fig. 5(a), reveals that the peak at $r \approx 5$ Å originates from pairs at $D = 2$ which are part of rings of length $L = 7$ and 8 . An example of the corresponding molecular arrangement is shown in Fig. 6(a). Since the length of a HB is strongly constrained around ≈ 2.8 Å, these types of configurations at $D = 2$ are associated to typical OOO angles of about 135° . Such large angles (compared to the tetrahedral one) propagate in the HB network, promoting the formation of $L \geq 7$ rings. The same strategy (Eq. 2) also allows us to associate the peak at ≈ 6 Å to pairs at $D = 4$ for different values of L ; the decomposition of $g_4(r)$ is reported in Fig. 5(b). Pairs at $r \approx 6$ Å are found in rings with a square-like segment such that they are almost-collinear with a third molecule, H-bonded to only one of them, as seen in Fig. 6(b). Pairs with $D = 4$ and $L = 8$ also provide a major contribution to the interstitial region with a crystal-clear peak shifting from 3.5 to 3.2 Å with increasing P , signaling a drastic network restructuring linked to the interpenetration of bond-coordination shells. An example of this local geometry is provided in Fig. 6(c). Movies S1–S3 included in the S.M. facilitate the visualization of these geometric arrangements.

In summary, by exploring with lengthy simulations the high-density liquid in TIP4P/Ice at $T = 188$ K

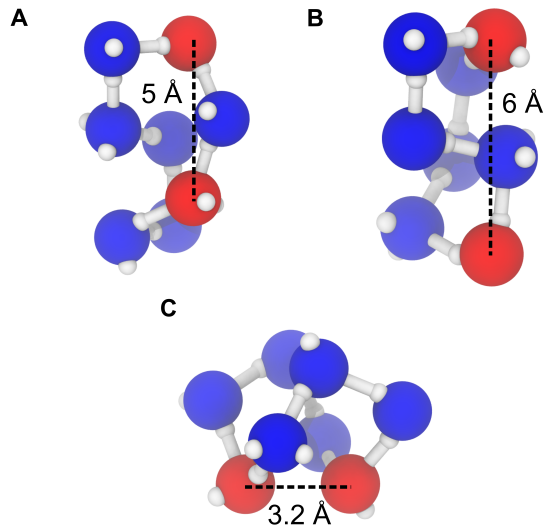


FIG. 6. Cartoon representation of the three local geometries that characterise water under high pressure: (a) pairs at $D = 2$ and $L = 8$ (D2L8) and (b,c) pairs with $D = 4$ and $L = 8$ (D4L8). D2L8 pairs are separated by a single molecule with a wide angle between the two HBs, and contribute to the $g(r)$ peak at $r \approx 5$ Å. D4L8 pairs contribute to the peaks at $r \approx 6$ Å and $r \approx 3.2$ Å. In the first case (b), the pair is almost-collinear with a third molecule H-bonded to only one of them; in the latter (c) the folding back of the ring allows the pair to get very close despite the large chemical distance.

(below the model liquid-liquid T_c), we have demonstrated that the liquid structure continuously evolves from eHDA to VHDA, supporting an interpretation of water high-density glasses based on thermodynamic continuity. Both eHDA and VHDA can be seen as the kinet-

ically arrested counterparts of a single high-density liquid, which is mirrored by eHDA close to the liquid-liquid transition pressure, and progressively more by VHDA as P is increased. Together with the experimentally established connection between the low density liquid and LDA [52, 53], our finding reinforces the hypothesis, based on the liquid-liquid critical point idea [31, 54, 55], that LDA and HDA-VHDA are the amorphous phases associated to the low and high density liquids, with no need to invoke a derailed crystallization pathway [28, 29].

We have also identified the geometrical origin of the structural changes taking place on going from eHDA to VHDA: (i) interstitial molecules arising from long rings with a “folded” structure, bringing molecules separated by three or four HBs close by in space; (ii) progressive distortion of the $\text{O}\ddot{\text{O}}\text{O}$ angle, favouring larger ring sizes (and responsible for the peak at $r \approx 5 \text{ \AA}$); (iii) specific structural motifs in rings of length $L \geq 8$ such that molecules separated by four HBs remain at distance $\approx 6 \text{ \AA}$.

We acknowledge discussions with Prof. Livia Bove and John Russo and support from MIUR PRIN 2017 (Project 2017Z55KCW). We also thank HPC-CINECA for providing computational resources.

-
- [1] O. Mishima and H. E. Stanley, *Nature* **396**, 329 (1998).
- [2] P. G. Debenedetti, *J. Phys.: Condens. Matter* **15**, 59 (2003).
- [3] K. Amann-Winkel, R. Böhmer, F. Fujara, C. Gainaru, B. Geil, and T. Loerting, *Rev. Mod. Phys.* **88**, 011002 (2016).
- [4] P. H. Handle, T. Loerting, and F. Sciortino, *Proc. Natl. Acad. Sci. USA* **114**, 13336 (2017).
- [5] H. Tanaka, *J. Chem. Phys.* **153**, 130901 (2020).
- [6] E. F. Burton and W. F. Oliver, *Proc. R. Soc. Lond. A* **153**, 166 (1935).
- [7] E. Mayer, *J. Appl. Phys.* **58**, 663 (1985).
- [8] K. Winkel, M. S. Elsaesser, E. Mayer, and T. Loerting, *J. Chem. Phys.* **128**, 044510 (2008).
- [9] D. T. Bowron, J. L. Finney, A. Hallbrucker, I. Kohl, T. Loerting, E. Mayer, and A. K. Soper, *J. Chem. Phys.* **125**, 194502 (2006).
- [10] P. H. Handle and T. Loerting, *J. Chem. Phys.* **148**, 124508 (2018).
- [11] O. Mishima, L. D. Calvert, and E. Whalley, *Nature* **310**, 393 (1984).
- [12] K. Amann-Winkel, C. Gainaru, P. H. Handle, M. Seidl, H. Nelson, R. Bohmer, and T. Loerting, *Proc. Natl. Acad. Sci. USA* **110**, 17720 (2013).
- [13] V. Fuentes-Landete, L. J. Plaga, M. Keppler, R. Böhmer, and T. Loerting, *Phys. Rev. X* **9**, 011015 (2019).
- [14] O. Mishima, *Nature* **384**, 546 (1996).
- [15] T. Loerting, C. Salzmänn, I. Kohl, E. Mayer, and A. Hallbrucker, *Phys. Chem. Chem. Phys.* **3**, 5355 (2001).
- [16] T. Loerting, K. Winkel, M. Seidl, M. Bauer, C. Mitterdorfer, P. H. Handle, C. G. Salzmänn, E. Mayer, J. L. Finney, and D. T. Bowron, *Phys. Chem. Chem. Phys.* **13**, 8783 (2011).
- [17] J. L. Finney, *Water: A Very Short Introduction*, first edition ed., Very Short Introductions No. 440 (Oxford University Press, Oxford, United Kingdom, 2015).
- [18] P. H. Handle and T. Loerting, *J. Chem. Phys.* **148**, 124509 (2018).
- [19] T. Loerting, C. G. Salzmänn, K. Winkel, and E. Mayer, *Phys. Chem. Chem. Phys.* **8**, 2810 (2006).
- [20] T. Loerting, W. Schustereder, K. Winkel, C. G. Salzmänn, I. Kohl, and E. Mayer, *Phys. Rev. Lett.* **96**, 025702 (2006).
- [21] C. G. Salzmänn, T. Loerting, S. Klotz, P. W. Mirwald, A. Hallbrucker, and E. Mayer, *Phys. Chem. Chem. Phys.* **8**, 386 (2006).
- [22] A. K. Soper and M. A. Ricci, *Phys. Rev. Lett.* **84**, 2881 (2000).
- [23] D. Mariedahl, F. Perakis, A. Späh, H. Pathak, K. H. Kim, G. Camisasca, D. Schlesinger, C. Benmore, L. G. M. Pettersson, A. Nilsson, and K. Amann-Winkel, *J. Phys. Chem. B* **122**, 7616 (2018).
- [24] H. Tanaka, H. Tong, R. Shi, and J. Russo, *Nat. Rev. Phys.* **1**, 333 (2019).
- [25] F. Martelli, F. Leoni, F. Sciortino, and J. Russo, *J. Chem. Phys.* **153**, 104503 (2020).
- [26] J. L. Finney, D. T. Bowron, A. K. Soper, T. Loerting, E. Mayer, and A. Hallbrucker, *Phys. Rev. Lett.* **89**, 205503 (2002).
- [27] K. Amann-Winkel, D. T. Bowron, and T. Loerting, *Mol. Phys.* **117**, 3207 (2019).
- [28] J. J. Shephard, S. Ling, G. C. Sosso, A. Michaelides, B. Slater, and C. G. Salzmänn, *J. Phys. Chem. Lett.* **8**, 1645 (2017).
- [29] C. A. Tulk, J. J. Molaison, A. R. MakhluF, C. E. Manning, and D. D. Klug, *Nature* **569**, 542 (2019).
- [30] J. S. Tse, D. D. Klug, C. A. Tulk, I. Swainson, E. C. Svensson, C.-K. Loong, V. Shpakov, V. R. Belosludov, R. V. Belosludov, and Y. Kawazoe, *Nature* **400**, 647 (1999).
- [31] P. H. Poole, F. Sciortino, U. Essmann, and H. E. Stanley, *Nature* **360**, 324 (1992).
- [32] N. Giovambattista, H. E. Stanley, and F. Sciortino, *Phys. Rev. E* **72**, 031510 (2005).
- [33] N. Giovambattista, H. E. Stanley, and F. Sciortino, *Phys. Rev. Lett.* **94**, 107803 (2005).
- [34] R. Martoňák, D. Donadio, and M. Parrinello, *J. Chem. Phys.* **122**, 134501 (2005).
- [35] P. H. Handle, F. Sciortino, and N. Giovambattista, *J. Chem. Phys.* **150**, 244506 (2019).
- [36] J. L. F. Abascal, E. Sanz, R. García Fernández, and C. Vega, *J. Chem. Phys.* **122**, 234511 (2005).
- [37] P. G. Debenedetti, F. Sciortino, and G. H. Zerze, *Science* **369**, 289 (2020).
- [38] R. Foffi, J. Russo, and F. Sciortino, *J. Chem. Phys.* **154**, 184506 (2021).
- [39] F. H. Stillinger, *Energy Landscapes, Inherent Structures, and Condensed-Matter Phenomena* (Princeton University Press, Princeton, New Jersey, 2015).
- [40] M. J. Abraham, T. Murtola, R. Schulz, S. Páll, J. C. Smith, B. Hess, and E. Lindahl, *SoftwareX* **1-2**, 19 (2015).
- [41] D. Frenkel and B. Smit, *Understanding Molecular Simulation from Algorithms to Applications* (Academic Press, San Diego, 2002).
- [42] M. Parrinello and A. Rahman, *J. Appl. Phys.* **52**, 7182 (1981).

- [43] B. Hess, H. Bekker, H. J. C. Berendsen, and J. G. E. M. Fraaije, *J. Comput. Chem.* **18**, 1463 (1997).
- [44] M. P. Allen and D. J. Tildesley, *Computer Simulation of Liquids*, second edition ed. (Oxford University Press, Oxford, 2017).
- [45] H. J. C. Berendsen, J. P. M. Postma, W. F. van Gunsteren, A. DiNola, and J. R. Haak, *J. Chem. Phys.* **81**, 3684 (1984).
- [46] R. Kumar, J. R. Schmidt, and J. L. Skinner, *J. Chem. Phys.* **126**, 204107 (2007).
- [47] S. Saito, B. Bagchi, and I. Ohmine, *J. Chem. Phys.* **149**, 124504 (2018).
- [48] J.-P. Hansen and I. R. McDonald, *Theory of Simple Liquids: With Applications of Soft Matter* (Elsevier, Academic Press, Amsterdam, 2013).
- [49] C. P. Herrero and R. Ramírez, *Phys. Rev. B* **84**, 224112 (2011).
- [50] C. P. Herrero and R. Ramírez, *J. Chem. Phys.* **137**, 104505 (2012).
- [51] A. Luzar and D. Chandler, *Nature* **379**, 55 (1996).
- [52] L. Kringle, W. A. Thornley, B. D. Kay, and G. A. Kimmel, *Science* **369**, 1490 (2020).
- [53] L. Kringle, W. A. Thornley, B. D. Kay, and G. A. Kimmel, *Proc. Natl. Acad. Sci. USA* **118**, e2022884118 (2021).
- [54] J. C. Palmer, P. H. Poole, F. Sciortino, and P. G. Debenedetti, *Chem. Rev.* **118**, 9129 (2018).
- [55] K. H. Kim, K. Amann-Winkel, N. Giovambattista, A. Späh, F. Perakis, H. Pathak, M. L. Parada, C. Yang, D. Mariedahl, T. Eklund, T. J. Lane, S. You, S. Jeong, M. Weston, J. H. Lee, I. Eom, M. Kim, J. Park, S. H. Chun, P. H. Poole, and A. Nilsson, *Science* **370**, 978 (2020).

**Supplementary Materials for: On the structure of high-pressure
supercooled and glassy water**

Riccardo Foffi and Francesco Sciortino

*Department of Physics, Sapienza Università di Roma,
Piazzale Aldo Moro, 5, 00185 Rome, Italy*

arXiv:2109.08766v1 [cond-mat.soft] 17 Sep 2021

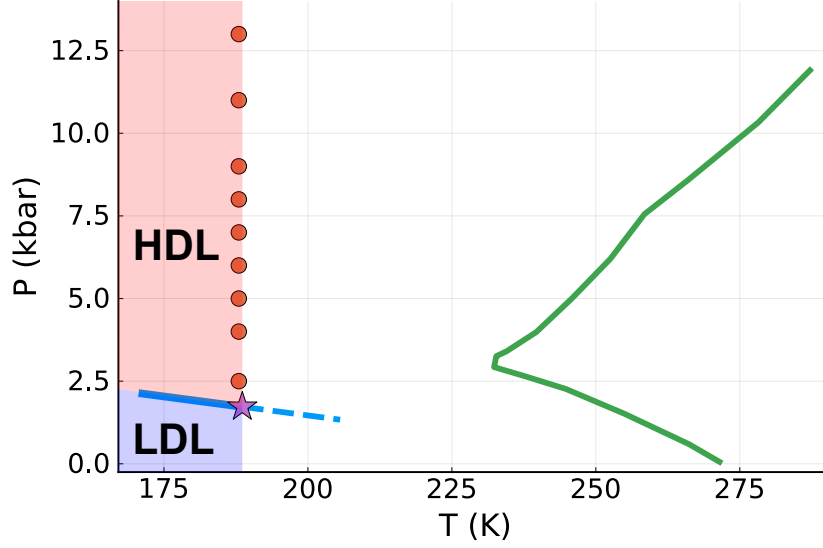


FIG. S1. P - T projection of the phase diagram of TIP4P/Ice, showing the explored state points (orange circles), the liquid-liquid critical point location estimated in Ref. [7] (violet star), the liquid-liquid transition line from Ref. [8] (solid blue line) and its extension in the supercritical regime (dashed blue line) and the solid-liquid coexistence curve from Ref. [1] (solid green line).

TABLE S1. Equilibration and production times of the MD simulations.

pressure / kbar	equilibration time / μ s	production time / μ s
2.5	5.0	5.0
4.0	6.0	6.5
5.0	13.0	12.0
6.0	7.0	8.0
7.0	15.5	12.0
8.0	13.0	10.0
9.0	15.0	12.0
11.0	14.0	12.0
13.0	14.0	12.0

DESCRIPTION OF THE SIMULATIONS

This study is based on a set of classical molecular dynamics (MD) simulations of $N = 1000$ water molecules interacting via the TIP4P/Ice potential [1] in the NPT ensemble, using

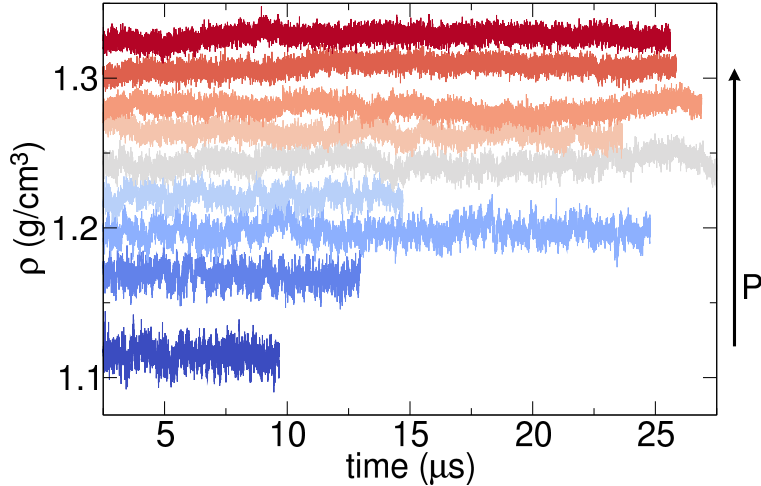


FIG. S2. Evolution of density in time along the 188 K isotherm. Colors from blue to red indicate increasing pressure from 2.5 to 13 kbar. The precise pressure values are listed in Table I.

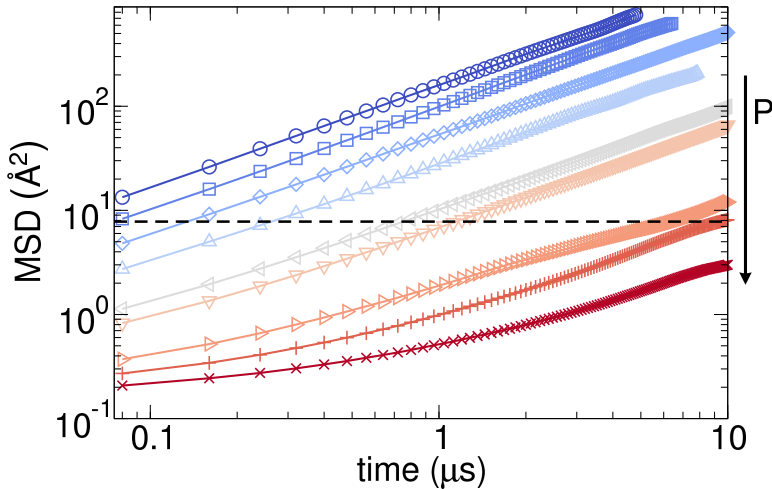


FIG. S3. Mean-square displacement of water molecules during the production phase of the MD simulations along the 188 K isotherm. Colors from blue to red indicate increasing pressure from 2.5 to 13 kbar. The precise pressure values are listed in Table I. The black dashed line at 7.8 \AA^2 represents the nearest-neighbour distance squared.

GROMACS 5.1.4 [2] in single precision. A cubic simulation box with periodic boundary conditions was adopted. We chose a leap-frog integrator with a timestep of 2 fs. Temperature coupling was controlled via a Nosé-Hoover thermostat [3] with a characteristic time of 8 ps, and pressure coupling was controlled via an isotropic Parrinello-Rahman barostat [4]

with characteristic time 18 ps. Molecular constraints were implemented via the LINCS algorithm [5] at the sixth order, and van der Waals forces have been evaluated with a cutoff distance of 0.9 nm. To account for electrostatic interactions the particle-mesh Ewald method at the fourth order, with real-space cutoff 0.9 nm [6] was selected.

In Fig. S1 we show the location of the state points explored in this work, with respect to other relevant features of the phase diagram of the TIP4P/Ice model. Equilibration and production times for these state points are reported in Table S1. The simulations at pressures 2.5 and 4 kbar have been reproduced from Ref. [8], but the latter has been significantly extended. The evolution of density with time throughout the whole simulation is shown in Fig. S2; also, the molecular mean square displacements during the production phase are reported in Fig. S3. Apart from the highest density (associated to pressure 13 kbar), molecules have diffused, on average, a distance larger than the nearest neighbour distance (the hydrogen bond length, $r \approx 2.8 \text{ \AA}$) during the production phase.

INHERENT STRUCTURES

We evaluated the inherent structures (IS) [9] by minimizing the potential energy via the steepest descent algorithm (STEEP) in GROMACS with a force tolerance of $1 \text{ J mol}^{-1} \text{ nm}^{-1}$ and a maximum step size $5 \times 10^{-4} \text{ nm}$. To ensure maximum accuracy, the minimization was carried in double precision. An example of the effect of the energy minimization on the liquid structure is shown in Fig. S4, for $P = 9 \text{ kbar}$. The increase in short-range order causes a significant increase in the height of the first peak, enhancing the separation between the first and second hydration shells. In the intermediate range, only minor differences are observed, related to a slight enhancement of peaks and valleys, while the long-range correlations are practically unaffected.

In Fig. S5 we also show the complete pressure dependence of the $g(r)$ in the real dynamics, to be compared with Fig. 2 in main text. It is evident that the process of energy minimization enhances the structural features of the system without artificially altering them.

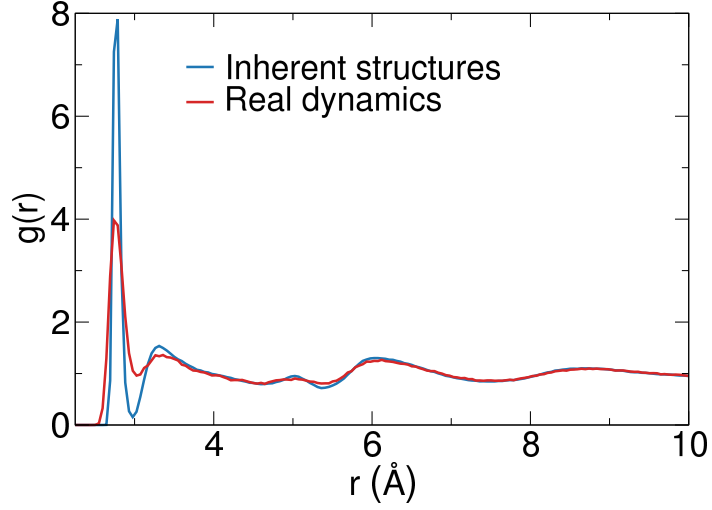


FIG. S4. Comparison of the radial distribution function of the liquid state ($T = 188$ K, $P = 9$ kbar) in the real dynamics and its inherent structures.

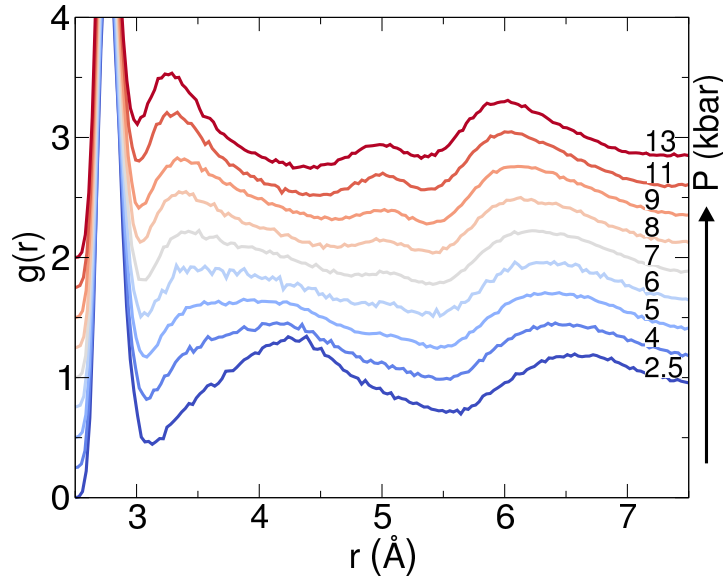


FIG. S5. Pressure dependence of the oxygen-oxygen $g(r)$ evaluated in the real dynamics along the 188 K isotherm. Successive $g(r)$ curves are shifted by 0.25 along the vertical axis.

STRUCTURE FACTOR

The structural description provided by the radial distribution function (Fig. 2 in main text) is here complimented by its Fourier transform, the structure factor $S(q)$ [10], reported in Fig. S6 (evaluated in the IS). In Fig. S7 $S(q)$ is evaluated in the real dynamics, and

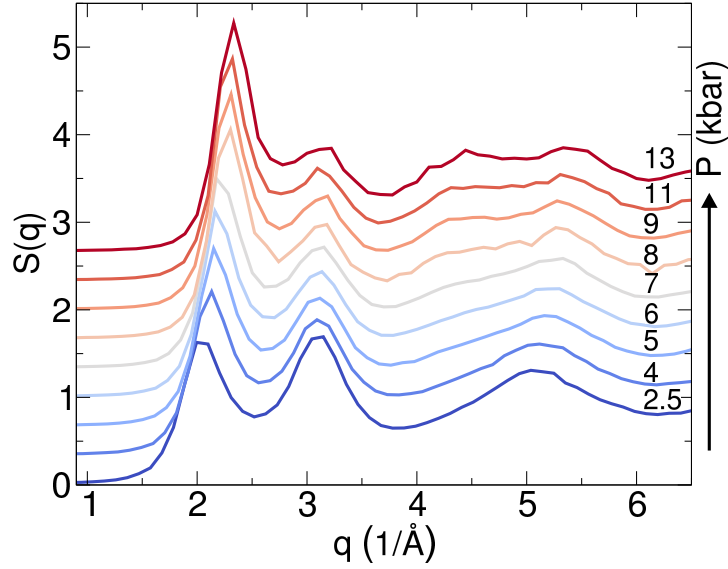


FIG. S6. Pressure dependence of the oxygen-oxygen structure factor evaluated in the IS along the 188 K isotherm. Successive $S(q)$ curves have been shifted by $1/3$ along the vertical axis.

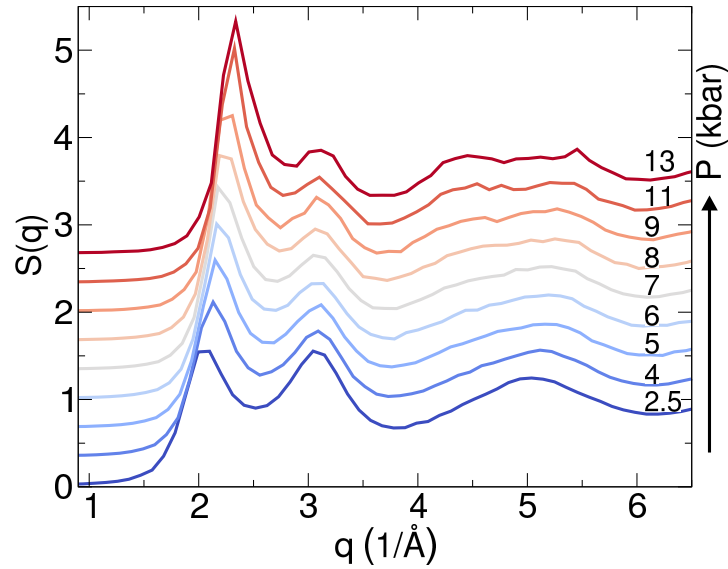


FIG. S7. Pressure dependence of the oxygen-oxygen structure factor evaluated in the real dynamics along the 188 K isotherm. Successive $S(q)$ curves have been shifted by $1/3$ along the vertical axis.

once again we observe that the structural features of the system are not altered by energy minimization. In Fourier space one observes a clear shift (and enhancement) of the pre-peak from ≈ 2 to $\approx 2.4 \text{ \AA}^{-1}$ and a decrease in the peak intensity at 3.1 \AA^{-1} . Also, above 7 kbar the peak around 5 \AA^{-1} splits into two broad but distinct peaks, at $\approx 4.5 \text{ \AA}^{-1}$ and

$\approx 5.5 \text{ \AA}^{-1}$ respectively. The evolution of these features is consistent with recent experimental observations by Mariedahl *et al.* [11], increasing our confidence in the ability of TIP4P/Ice to faithfully describe the structural properties of deep supercooled water.

COMPARISON WITH EXPERIMENTAL DATA

To obtain amorphous states that could be compared with the experimental glasses as shown in Fig. 3 of main text, the IS were annealed to 80 K and relaxed to ambient pressure. The annealing was carried out over an interval of 200 ps, and we used the Berendsen algorithm [12] for both temperature and pressure coupling with short relaxation times, respectively 0.8 and 1.8 ps. Here we adopted these algorithms to avoid artificial oscillations in T and P which are sometimes observed with other thermostats and barostats after abrupt changes in thermodynamic conditions. The Berendsen algorithm is known to provide the correct thermodynamics and structural averages, but incorrect fluctuations.

As explained in main text, the glass structures thus obtained are still not ready to be compared with experimental data; at such low temperatures quantum effects become relevant [13] and a correction, accounting for the delocalization of O atoms, has to be applied to the numerical results from the classical TIP4P/Ice potential. Fig. 3 shows the comparison of numerical and experimental data, after the numerical $g(r)$ has been convoluted with a Gaussian of variance $7.1 \times 10^{-3} \text{ \AA}^2$ as discussed in the main article; in Fig. S8 we compare the $g(r)$ before and after such correction is applied, for the glasses recovered at three different values of density. As expected, the convolution affects only the region of the first peak, while the correlations at larger separations are unaffected (although the curve is obviously smoothed).

HYDROGEN BONDS

To perform an accurate analysis based on topological properties it is of fundamental importance to correctly identify HBs at all thermodynamic conditions. Several different definitions of HB have been proposed throughout the years [14].

The definition of Luzar and Chandler [15] (LC) ($r_{\text{OO}} < 3.5 \text{ \AA}$ and $\theta < 30^\circ$ where θ is the (smallest) $\text{H}\hat{\text{O}}\cdots\text{O}$ angle) when applied to the IS allows us to identify HBs with high

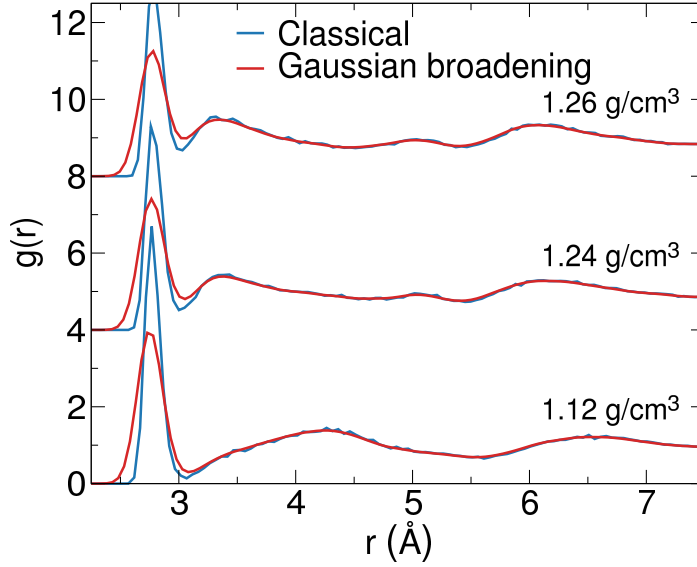


FIG. S8. Comparison of numerical $g(r)$ before and after application of quantum broadening corrections, for amorphous configurations at three different densities.

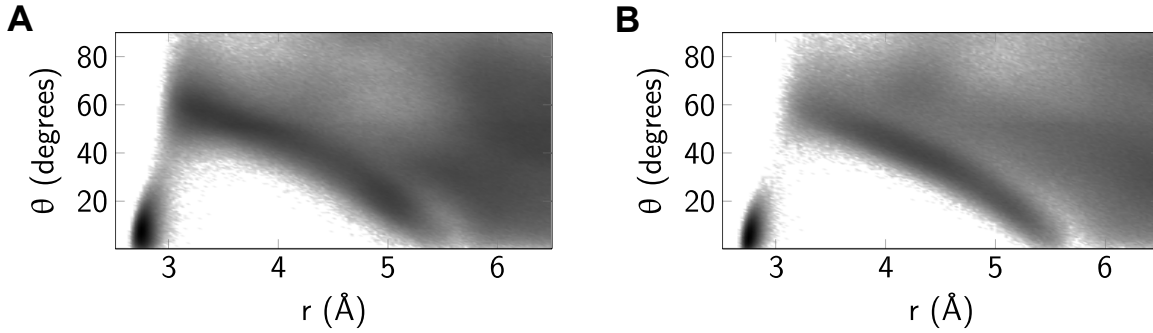


FIG. S9. Spatial density function, $g(r, \theta)$, of the OO distance r and the $\widehat{\text{HO}}\cdots\text{O}$ angle θ at (a) 13 kbar and (b) 2.5 kbar. The value of $g(r, \theta)$ is represented by intensity in logarithmic scale, increasing from white to black.

accuracy, despite the increasing distortion in the local environments that is observed upon isothermal compression. Figure S9 depicts the $g(r, \theta)$ distribution of the system at 2.5 and 13 kbar. With increasing pressure, the identification of HBs provided by the LC definition becomes less accurate since the distribution around the main HB peak ($r \approx 2.8 \text{ \AA}$, $\theta \approx 5^\circ$) becomes broader. It should be noticed, however, that point density in Fig. S9 is shown in log scale, so that low-probability regions in $r - \theta$ space are accentuated with respect to high-probability ones.

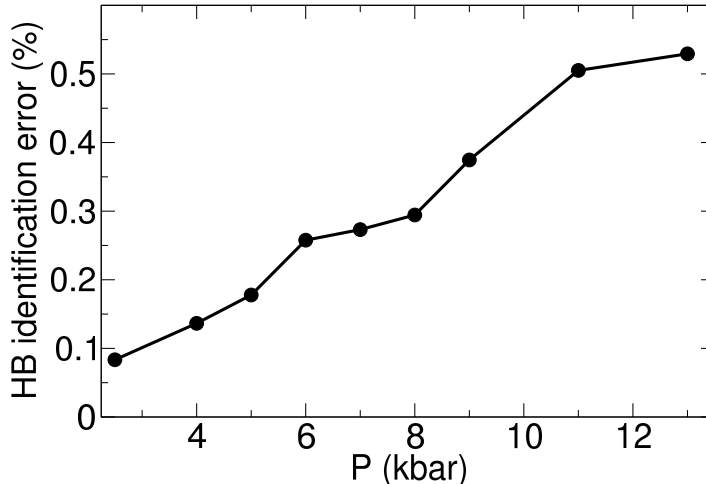


FIG. S10. Average identification error of HBs as a function of pressure with the Luzar-Chandler definition.

The average identification error committed by adopting the LC definition can be estimated as follows. We can consider “proper” HBs those that satisfy the LC conditions, and “uncertain” HBs those with a bond length $r < 3.5 \text{ \AA}$ but with an angle within 20% above the LC angular threshold: $30^\circ < \theta < 36^\circ$. It appears likely that at least a fraction of these uncertain bonds should be considered as proper HBs. The error can then be defined as the ratio between the number of uncertain and proper HBs. The results are reported in Fig. S10, showing that the average error is below 1% even at the highest pressure. The LC definition of HB is therefore reasonably valid over the whole isotherm.

To investigate an alternative definition, instead of using the LC angular threshold $\theta^* = 30^\circ$, we choose a r -dependent angular threshold $\theta^* = \theta^*(r)$ with the aim of minimizing the error intrinsic in the definition. The simplest approach uses a linear dependence, $\theta^*(r) = \theta_0 + \alpha r$. We thus identify a potential of mean force PMF (per unit thermal energy)

$$PMF = -\ln g(r, \theta) \quad (S1)$$

and obtain the values of θ_0 and α by identifying the linear path of maximum PMF passing through the saddle point at $r \approx 3 \text{ \AA}$ and $\theta \approx 35^\circ$. This path identifies the optimal boundary between H-bonded and non-H-bonded pairs. By optimising over the data at $P = 13 \text{ kbar}$, we find:

$$\theta_0 \approx 113^\circ, \quad \alpha \approx -26^\circ \text{ \AA}^{-1}. \quad (S2)$$

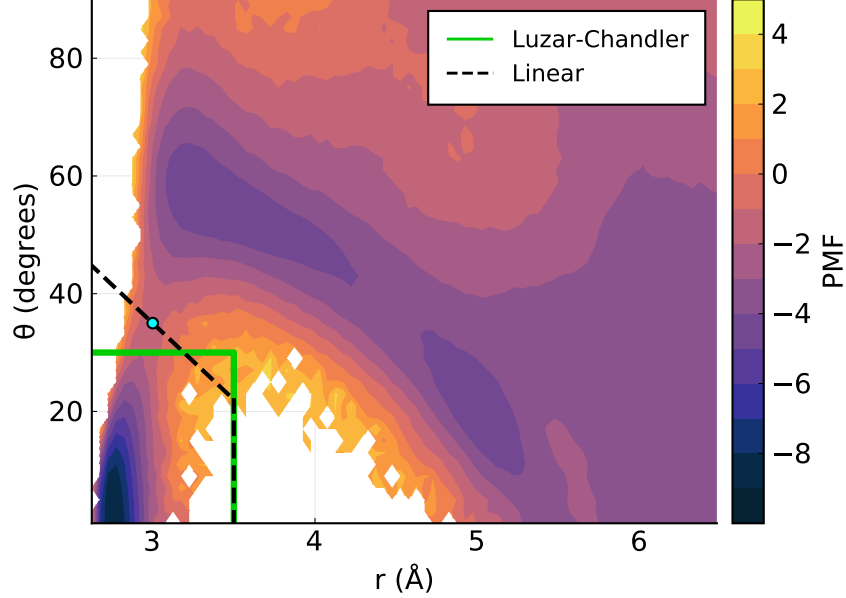


FIG. S11. Comparison, at $P = 13$ kbar, of the Luzar-Chandler definition of HB and the new definition obtained by evaluating the linear path ($\theta = \theta_0 + \alpha r$) of maximum PMF through the saddle point (cyan circle, found approximately at $r \approx 3 \text{ \AA}$ and $\theta \approx 35^\circ$).

With this method, two molecules are H-bonded if their O–O distance is $r < 3.5 \text{ \AA}$ and their $\text{H}\hat{\text{O}}\cdots\text{O}$ angle satisfies $\theta < 113^\circ - 26^\circ \text{ \AA}^{-1} r$. See Fig. S11. At $P = 13$ kbar, where the difference between the two definitions is largest, the new definition counts an average of ≈ 2002 H-bonded pairs out of 1000 molecules, whereas the LC criterion identifies ≈ 1995 pairs; that is, an average difference of 7 HBs per configuration. As the pressure is decreased, the difference between the two definitions decreases. Given the minute difference, we conclude that even in this high- P regime, the LC definition can be adopted without the risk of significantly compromising the topological description of the system. Hydrogen bonds in the following (and in the main text) are thus always identified according to the LC definition in the IS.

NETWORK DEFECTS

In the explored thermodynamic range, we observe molecules with coordination numbers 3 or 5 (network defects); Following the nomenclature introduced by Saito *et al.* [16], 5-coordinated defects donate 2 HBs and accept 3 (H^2O^3), while 3-coordinated defects can either donate 2 HBs and accept 1 (H^2O^1) or donate 1 and accept 2 (H^1O^2). In a previous

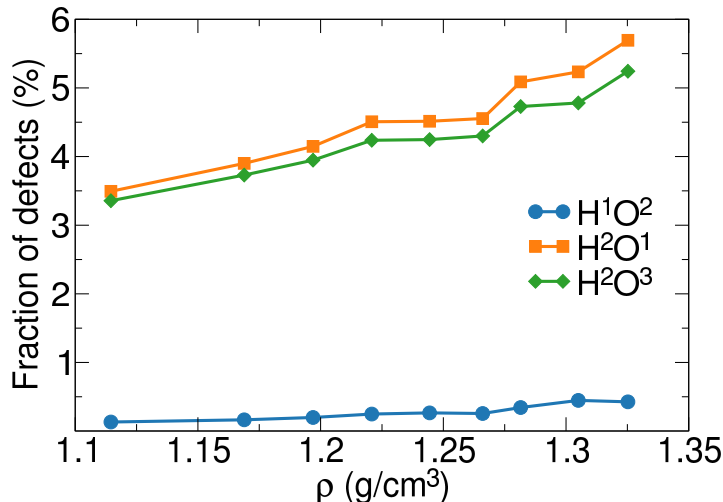


FIG. S12. Population of network defects as a function of density.

work [8] we have shown that network defects appear to have a role in the structural transformations that characterize the liquid-liquid phase transition of (TIP4P/Ice) water; along the 188 K isotherm, from ambient pressure up to 2.5 kbar, H²O¹ and H²O³ were found to be almost-perfectly paired, thus conserving the total number of HBs and imposing only a minor energetic cost on the system; the presence of H¹O², a geometry that sacrifices a HB, was negligible.

The fraction of defects, distinguished by species, that we observed along the 188 K isotherm from 2.5 to 13 kbar is shown in Fig. S12. At all pressures, more than 99.5% of the H atoms are involved in HBs, indicating that, despite the high pressure and intense structural distortion, practically all molecules donate two hydrogens for bonding. While most molecules still participate in four HBs, there is a fraction of network defects, accepting either one or three bonds, whose concentration increases (roughly) linearly with density. The strong correlation between the number of five- and three-coordinated molecules and the density might suggest that the primary effect of compression is to convert a pair of tetrahedrally-coordinated molecules into a H²O¹ – H²O³ defect pair. Consistent with the weak dependence of E on ρ (see Fig. 1 of the main text), such a transformation does not have a significant energetic cost, preserving the total number of HBs while improving the packing.

The structural properties of network defects in this thermodynamic regime are also consistent with the observations made in Ref. [8]. Figure S13 shows the contribution to the $g(r)$

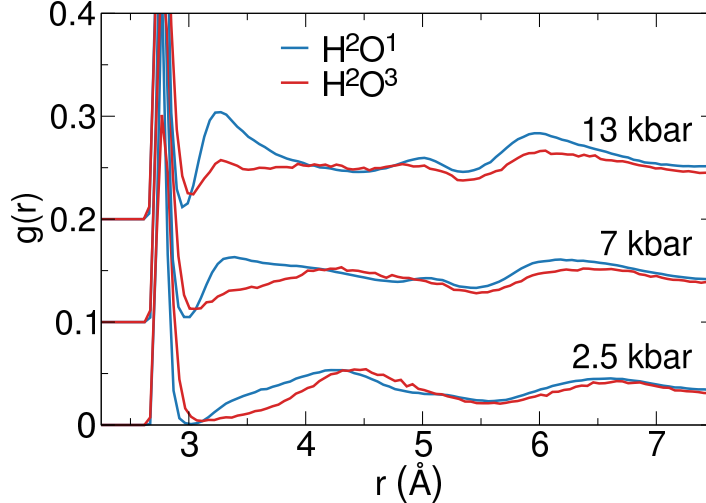


FIG. S13. Contribution of network defects to $g(r)$ evaluated in the IS at three different pressures along the 188 K isotherm. Curves were shifted by 0.1 along the vertical axis; the $r \rightarrow \infty$ limit indicates the relative concentration of the associated defect species.

from network defects at three different pressures; the two curves represent the radial structure around H_2O^1 and H_2O^3 molecules, respectively. It is therefore clear that 3-coordinated molecules participate actively in the interpenetration phenomenon, while 5-coordinated ones display an increasingly featureless distribution as P increases.

TOPOLOGY AND STRUCTURE

The core results about the structure of the system are obtained by classifying the pairs of molecules in the system according to their chemical distance and ring length, as outlined in the main text. The definition of ring that we adopted here is the same that we proposed in Ref. [8]. For a given pair of molecules (i, j) at chemical distance D , the ring length L associated to this pair is the length (measured in steps along the HB network) of the closed path obtained by joining the two shortest non-intersecting HB-paths between i and j . By definition, $L \geq 2D$.

With this approach, we first separate all pairs of molecules in the system depending on their chemical distances D , so as to evaluate the contribution to the radial distribution

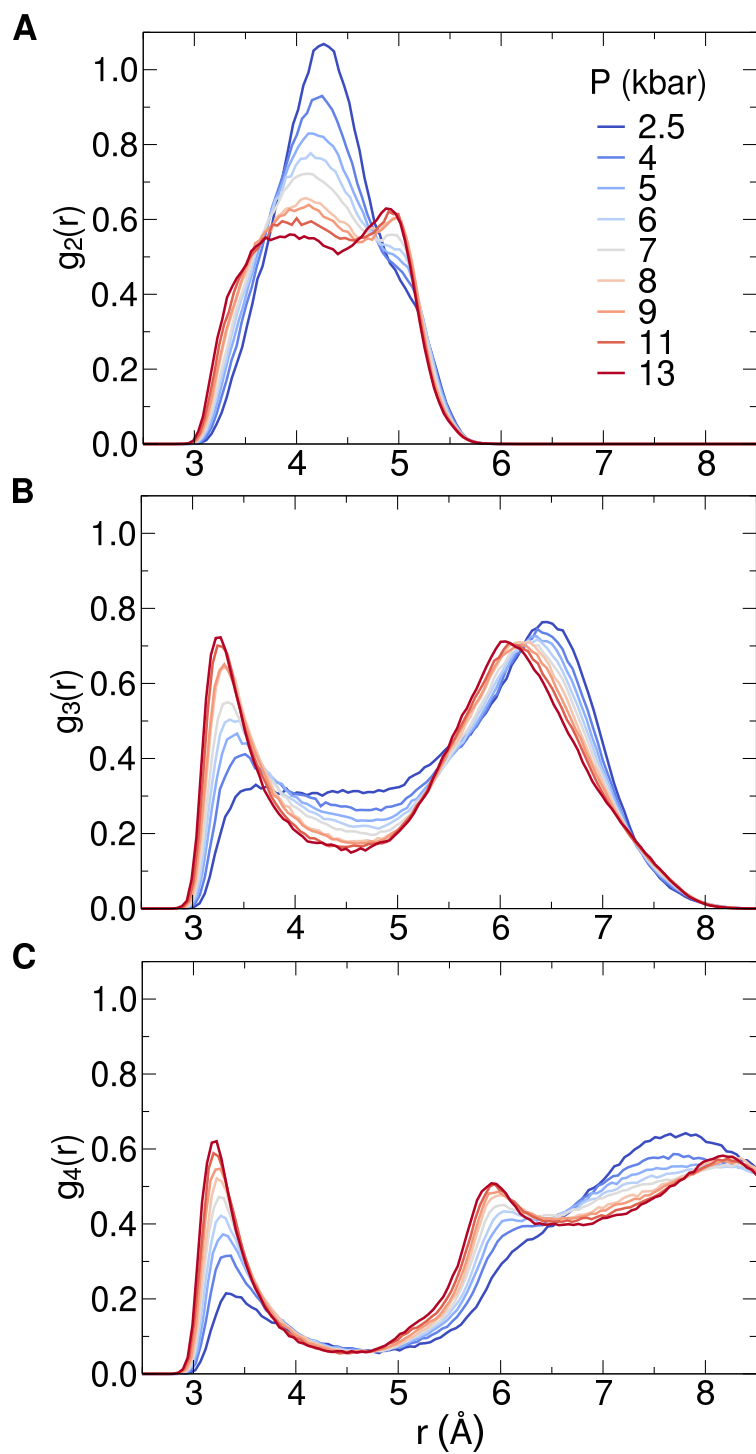


FIG. S14. Contributions to the $g(r)$ along the 188 K isotherm separated by coordination shells: (a) $D = 2$, (b) $D = 3$, (c) $D = 4$. Pressure increases from blue to red.

function $g(r)$ arising from pairs at chemical distance D , such that

$$g(r) = \sum_D g_D(r).$$

The results of this decomposition at pressures 2.5 and 13 kbar are shown in Fig. 4 of the main text; here, in Fig. S14 we report the complete pressure dependence of the g_D contributions (for $D = 2, 3, 4$) along the 188 K isotherm.

As a second step, each pair of molecules at chemical distance D is further characterized in terms of its ring length L ; the total structure of the system is now decomposed in such a way that

$$g(r) = \sum_D \sum_L g_D^L(r).$$

Fig. S15 shows a sample HB network, where two different pairs of molecules are highlighted, in blue and red respectively. The ring length associated to the blue pair (a) is $L = 6$, and that associated to the red pair (b) is $L = 8$; the two pairs are characterized by different ring lengths, despite the fact that the blue molecules are included in the ring that connects the red pair.

The pressure dependence of each g_D^L along the isotherm is shown in Figs. S16–S18. The behavior of g_2 and g_4 (and their components g_2^L and g_4^L) is extensively discussed in the main text. Besides the increase in the interstitial peak, g_3 does not show clear relevant features in the evolution from high to very-high densities. As seen in Fig. S17, the (small) increase in the g_3 contribution at $r \approx 6 \text{ \AA}$ can be ascribed fundamentally to the g_3^8 component, where a peak continuously shifting from $\approx 6.5 \text{ \AA}$ to $\approx 6 \text{ \AA}$ is observed, without evidence of significant transformations in the underlying network structure.

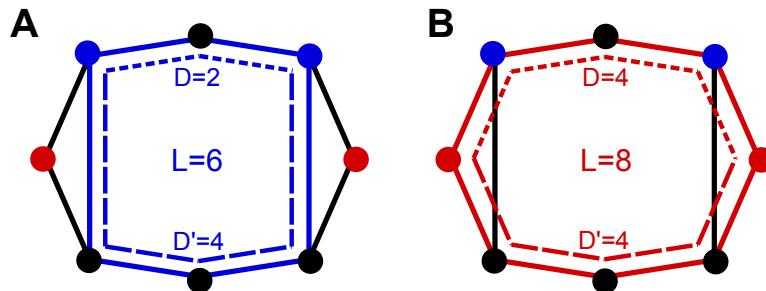


FIG. S15. Sample schematics of a HB network showing how rings and ring lengths are identified. (a) The blue molecules are at chemical distance $D = 2$ (short-dashed path), and the second-shortest path (long-dashed) has length $D' = 4$; by joining these two paths we obtain a ring of length $L = 6$. (b) The two shortest paths between the pair of red molecules are both of length 4, producing a ring of length $L = 8$.

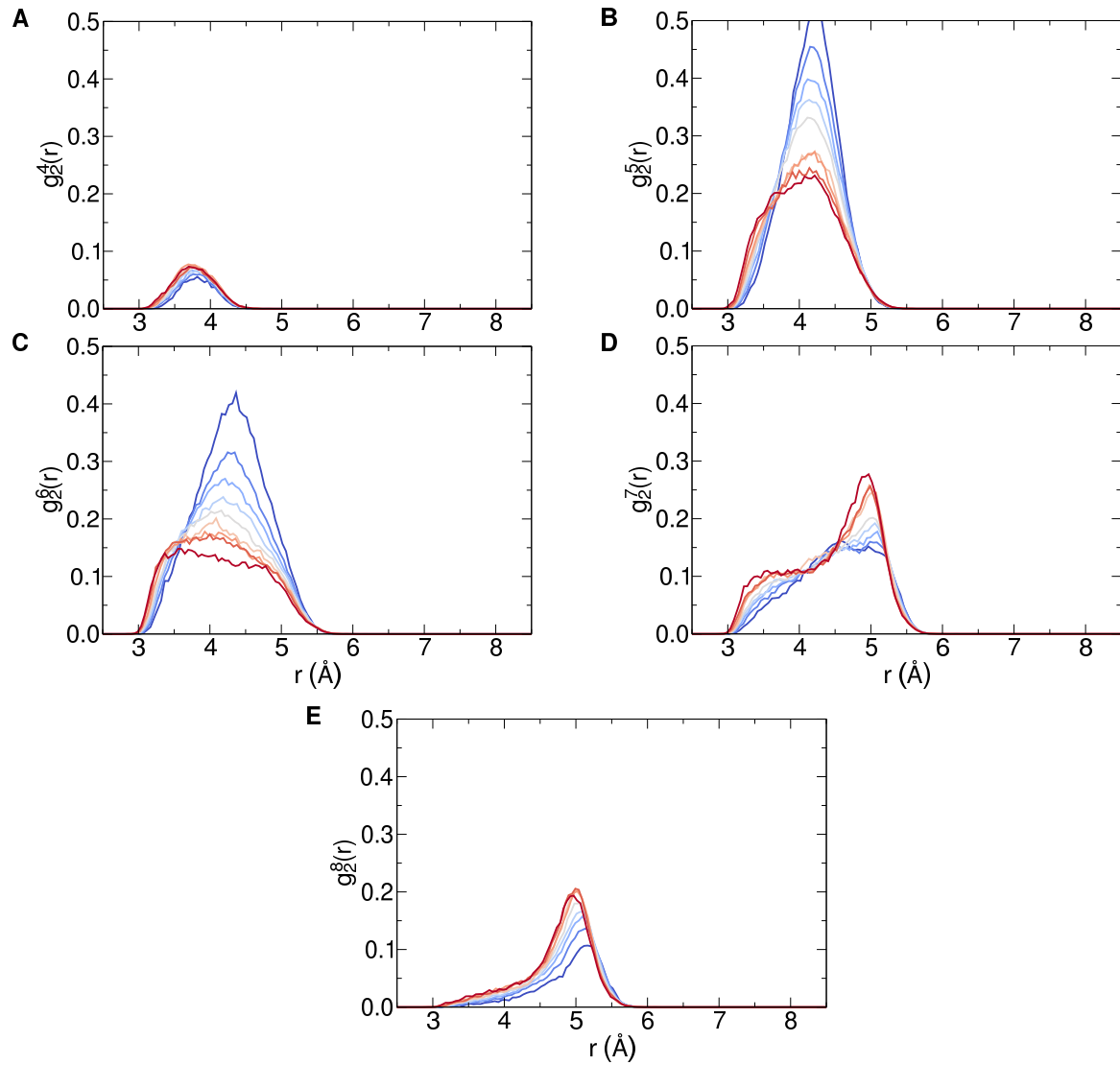


FIG. S16. Contributions to the $g(r)$ arising from pairs of molecules at chemical distance $D = 2$ in rings of length L ranging from (a) $L = 4$ to (e) $L = 8$. Pressure increases from blue to red.

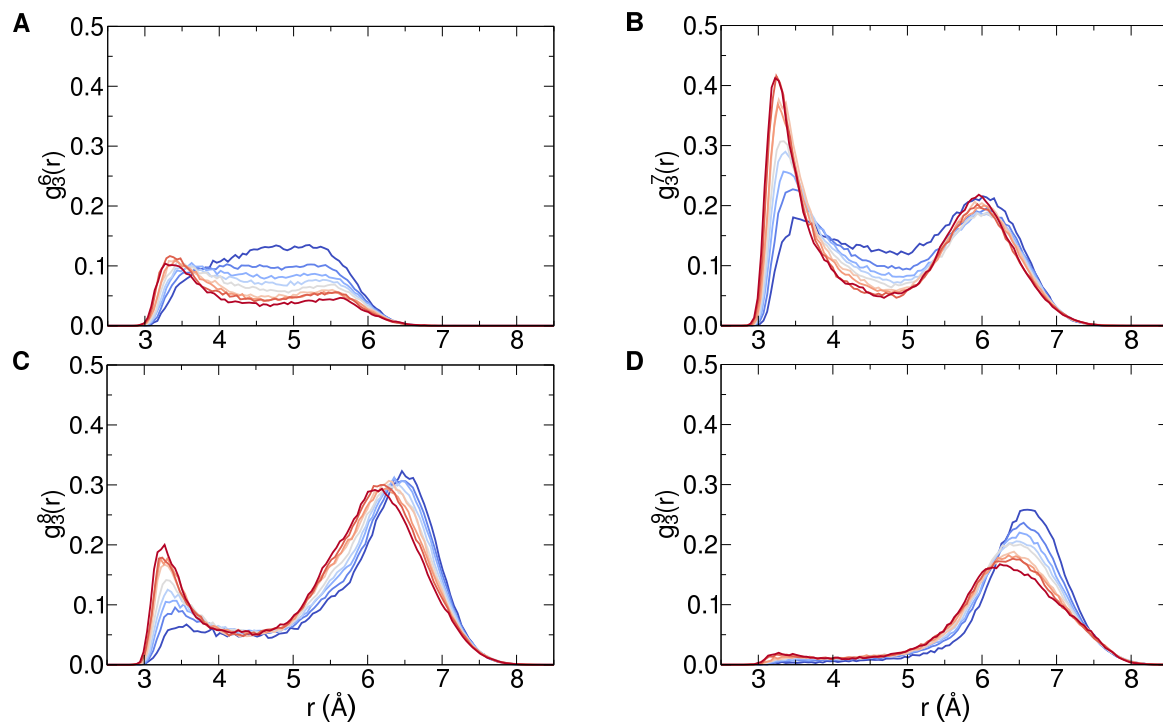


FIG. S17. Contributions to the $g(r)$ arising from pairs of molecules at chemical distance $D = 3$ in rings of length L ranging from (a) $L = 6$ to (d) $L = 9$. Pressure increases from blue to red.

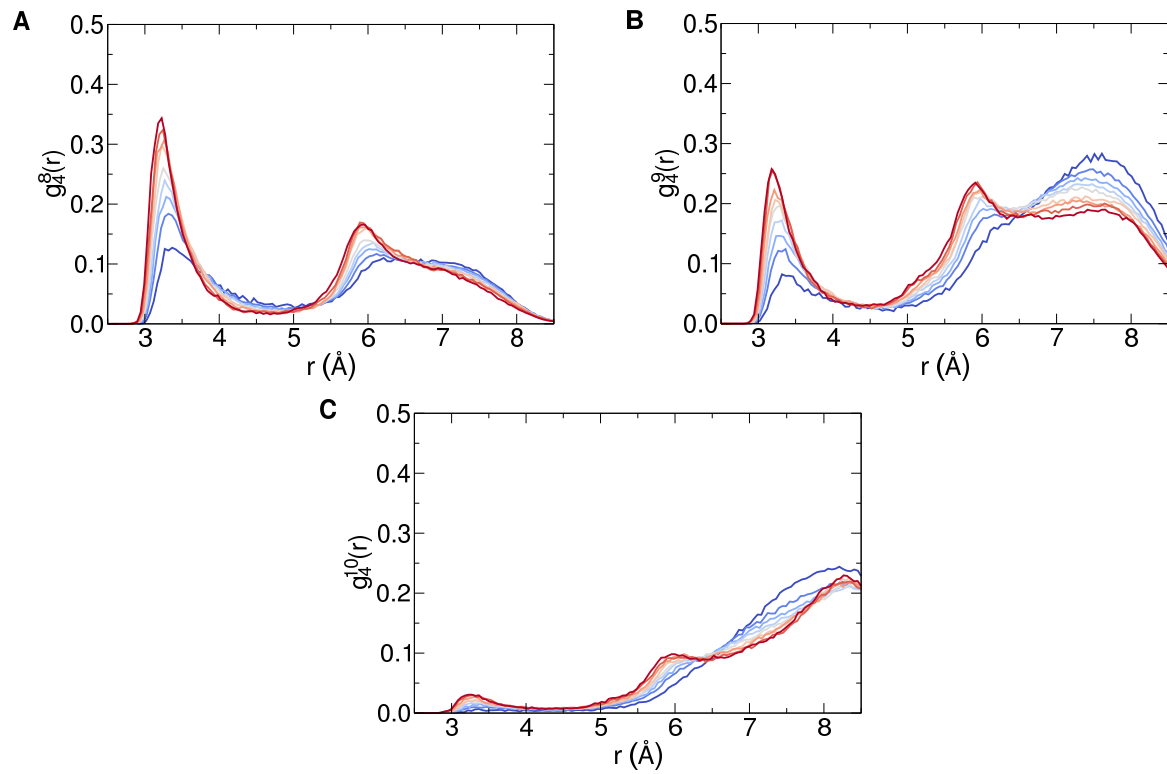


FIG. S18. Contributions to the $g(r)$ arising from pairs of molecules at chemical distance $D = 4$ in rings of length L ranging from (a) $L = 8$ to (c) $L = 10$. Pressure increases from blue to red.

-
- [1] J. L. F. Abascal, E. Sanz, R. García Fernández, and C. Vega, *J. Chem. Phys.* **122**, 234511 (2005).
- [2] M. J. Abraham, T. Murtola, R. Schulz, S. Páll, J. C. Smith, B. Hess, and E. Lindahl, *SoftwareX* **1-2**, 19 (2015).
- [3] D. Frenkel and B. Smit, *Understanding Molecular Simulation from Algorithms to Applications* (Academic Press, San Diego, 2002).
- [4] M. Parrinello and A. Rahman, *J. Appl. Phys.* **52**, 7182 (1981).
- [5] B. Hess, H. Bekker, H. J. Berendsen, and J. G. Fraaije, *J. Comput. Chem* **18**, 1463 (1997).
- [6] M. P. Allen and D. J. Tildesley, *Computer Simulation of Liquids*, second edition ed. (Oxford University Press, Oxford, 2017).
- [7] P. G. Debenedetti, F. Sciortino, and G. H. Zerze, *Science* **369**, 289 (2020).
- [8] R. Foffi, J. Russo, and F. Sciortino, *J. Chem. Phys.* **154**, 184506 (2021).
- [9] F. H. Stillinger, *Energy Landscapes, Inherent Structures, and Condensed-Matter Phenomena* (Princeton University Press, Princeton, New Jersey, 2015).
- [10] J.-P. Hansen and I. R. McDonald, *Theory of Simple Liquids: With Applications of Soft Matter* (Elsevier, Academic Press, Amsterdam, 2013).
- [11] D. Mariedahl, F. Perakis, A. Späh, H. Pathak, K. H. Kim, G. Camisasca, D. Schlesinger, C. Benmore, L. G. M. Pettersson, A. Nilsson, and K. Amann-Winkel, *J. Phys. Chem. B* **122**, 7616 (2018).
- [12] H. J. C. Berendsen, J. P. M. Postma, W. F. van Gunsteren, A. DiNola, and J. R. Haak, *J. Chem. Phys.* **81**, 3684 (1984).
- [13] C. P. Herrero and R. Ramírez, *J. Chem. Phys.* **137**, 104505 (2012).
- [14] R. Kumar, J. R. Schmidt, and J. L. Skinner, *J. Chem. Phys.* **126**, 204107 (2007).
- [15] A. Luzar and D. Chandler, *Nature* **379**, 55 (1996).
- [16] S. Saito, B. Bagchi, and I. Ohmine, *J. Chem. Phys.* **149**, 124504 (2018).